ATMOSPHERIC SCIENCE

Attribution of individual methane and carbon dioxide emission sources using EMIT observations from space

Andrew K. Thorpe[1]*, Robert O. Green[1], David R. Thompson[1], Philip G. Brodrick[1], John W. Chapman[1], Clayton D. Elder[1], Itziar Irakulis-Loitxate[2,3], Daniel H. Cusworth[4,5], Alana K. Ayasse[4,5], Riley M. Duren[1,4,5], Christian Frankenberg[6], Luis Guanter[2,7], John R. Worden[1], Philip E. Dennison[8], Dar A. Roberts[9], K. Dana Chadwick[1], Michael L. Eastwood[1], Jay E. Fahlen[1], Charles E. Miller[1]

Carbon dioxide and methane emissions are the two primary anthropogenic climate-forcing agents and an important source of uncertainty in the global carbon budget. Uncertainties are further magnified when emissions occur at fine spatial scales (<1 km), making attribution challenging. We present the first observations from NASA's Earth Surface Mineral Dust Source Investigation (EMIT) imaging spectrometer showing quantification and attribution of fine-scale methane (0.3 to 73 tonnes CH_4 hour^{-1}) and carbon dioxide sources (1571 to 3511 tonnes CO_2 hour^{-1}) spanning the oil and gas, waste, and energy sectors. For selected countries observed during the first 30 days of EMIT operations, methane emissions varied at a regional scale, with the largest total emissions observed for Turkmenistan (731 ± 148 tonnes CH_4 hour^{-1}). These results highlight the contributions of current and planned point source imagers in closing global carbon budgets.

INTRODUCTION

Carbon dioxide (CO_2) and methane (CH_4) are the two primary anthropogenic climate-forcing agents. Fossil carbon dioxide emissions are rapidly becoming the largest source of uncertainty in the global carbon budget because of increasing emissions in areas with poor reporting requirements (*1*). Global inventories of fossil carbon dioxide emissions rely on activity data and have an estimated uncertainty in excess of 0.5 billion (metric) tonnes of C (Gt C) year^{-1} (*2*). Uncertainties vary considerably between those countries with mature reporting requirements and data transparency from a few percent (*3*) to much larger uncertainties (15 to 18%) for countries such as China (*4*, *5*). Carbon dioxide emissions from stationary sources (e.g., power plants, cement production, and refineries) make up approximately one-third of the anthropogenic budget (*6*), and the location and magnitude of large point sources contribute to uncertainty in gridded inventories (*7*). Reducing uncertainty from these sources offers the potential to reconcile global fossil carbon dioxide emissions.

For global methane emissions, bottom-up inventory uncertainties range between 20 and 35% for the agriculture, waste, and fossil fuel sectors; 50% for biomass burning and natural wetland emissions; and 100% or higher for natural sources such as geological seeps and inland waters (*8*). Large uncertainties remain regarding partitioning between these sources and the cause of recent changes in the atmospheric growth rate of methane (*9*, *10*). Current best estimates place anthropogenic methane emissions at around half of total methane emissions (*8*). Because the methane lifetime in the atmosphere is only about 10 years (mean of 9.8 ± 1.6 years) (*11*) and methane is more efficient at trapping radiation than carbon dioxide, targeting reductions in anthropogenic methane emissions offers an effective approach to decrease overall atmospheric radiative forcing.

Satellite instruments measuring atmospheric methane and carbon dioxide in the shortwave infrared include area flux mappers and point source imagers with complementary attributes (*12*). With coarse spatial resolution (0.1 to 10 km), area flux mappers such as the Tropospheric Monitoring Instrument (TROPOMI) (*13*) and the Orbiting Carbon Observatory (OCO) instruments (*14*) are best suited to quantify methane and carbon dioxide emissions on regional to global scales. Because of fine spatial resolutions (typically ≤60 m), point source imagers can resolve individual point sources down to the range of 0.1 to 10 tonnes CH_4 hour^{-1} and attribute emissions to specific sectors. The first observation of a methane point source from space used the Hyperion imaging spectrometer for the 2015 Aliso Canyon blowout (*15*). Since 2016, the GHGSat constellation of Fabry-Perot interferometers has identified methane point sources at coal mine vents (*16*), the oil and gas sector (*17*), and landfills (*18*). The PRISMA imaging spectrometer, focused primarily on measuring Earth surface properties, has recently been used to quantify methane point source emissions from a gas well blowout (*19*), as well as oil and gas and coal mine emissions (*20*). Multiband imagers, such as Sentinel-2 (*21*, *22*), WorldView-3 (*23*), and Landsat-8 (*24*), have also been able to identify similar source types.

The Earth Surface Mineral Dust Source Investigation's (EMIT) (*25*, *26*) core technology and potential greenhouse gas mapping capability were first demonstrated using visible to shortwave infrared airborne imaging spectrometers developed at the Jet Propulsion Laboratory (JPL). The Airborne Visible/Infrared Imaging Spectrometer (AVIRIS) (*27*) mapped the first remotely sensed methane point source plume at the Coal Oil Point seeps offshore of Santa Barbara, California (*28*), followed by emissions at the

[1]Jet Propulsion Laboratory, California Institute of Technology, Pasadena, CA, USA. [2]Universitat Politècnica de València (UPV), Valencia, Spain. [3]International Methane Emissions Observatory, United Nations Environment Programme, Paris, France. [4]Carbon Mapper, Pasadena, CA, USA. [5]University of Arizona, Tucson, AZ, USA. [6]California Institute of Technology, Pasadena, CA, USA. [7]Environmental Defense Fund, Amsterdam, 1017, Netherlands. [8]University of Utah, Salt Lake City, UT, USA. [9]University of California, Santa Barbara, Santa Barbara, CA, USA.
*Corresponding author. Email: andrew.k.thorpe@jpl.nasa.gov

Inglewood Oilfield in Los Angeles County (*29*) and the Aliso Canyon blowout (*30*). The next-generation instruments, AVIRIS-NG (*31*) and the Global Airborne Observatory (GAO) (*32*), have surveyed the oil and gas sector in the Four Corners Region (*33*); the Permian (*34*); the Uinta, Denver-Julesburg, and Marcellus basins (*35*); and the Gulf of Mexico (*36*) of the United States. In addition, methane plumes were identified in Canada (*37*) and India (*38*). Methane emissions have also been characterized for the waste (*38*, *39*) and agricultural sectors (*40*, *41*), as well as numerous methane emission hotspots identified in thawing permafrost regions of Alaska and Canada (*42*, *43*). Results from airborne studies using AVIRIS-NG and GAO across multiple source sectors (oil and gas, coal, livestock, and waste) indicate that methane point sources are often considerable contributors to net regional emissions, ranging between 13 and 67% of the total for some areas in the United States (*35*). Carbon dioxide emissions have also been mapped with AVIRIS (*44*), AVIRIS-NG (*45*), GAO, and PRISMA (*19*, *46*).

While limited in spatial coverage, this previous work demonstrates the utility of airborne imaging spectrometers to identify and quantify methane and carbon dioxide point sources and to prioritize mitigation efforts. In addition to the greenhouse gas application, these instruments have been used for remote sensing of Earth′s surface, including mineral (*47*, *48*), ecosystems (*49*, *50*), water quality (*51*, *52*), and snow and ice applications (*53*, *54*). Demonstration of these varied science applications with airborne imaging spectrometers laid the groundwork for the EMIT mission.

EMIT was launched on 14 July 2022 and is currently operating on the International Space Station (ISS). This imaging spectrometer measures reflected solar radiation from the visible to shortwave infrared and was designed to determine the mineral composition of arid, dust source regions and their influence on global radiative forcing. EMIT measures 285 distinct wavelengths at 7.4-nm spectral sampling between 381 and 2493 nm, including prominent methane and carbon dioxide absorption features in the shortwave infrared. EMIT features a 1242-element swath at approximately 60-m image pixel resolution. EMIT has demonstrated exceptionally high performance, with a spectral uniformity greater than 98% and a signal-to-noise ratio (SNR) ranging from 500 to 750 for most wavelengths at the US Geological Survey (USGS) Libya 4 calibration site (*55*). Compared to other point source imagers, EMIT provides a unique combination of high SNR and large 80-km swath, which enables an average daily coverage of 1.3×10^6 km^2, equivalent to the area of the Republic of South Africa. This unique combination of wide coverage, fine spatial resolution, high SNR, and excellent spectral uniformity distinguishes EMIT from other imaging spectrometers and makes it particularly well suited for identifying methane and carbon dioxide emissions. While focusing on coverage of arid lands, EMIT will map broad regions of Earth′s surface at latitudes from +51.6° to −51.6° (Fig. 1), which is dictated by the inclined, equatorial orbit of the ISS. EMIT should complete its primary mission by September 2023, and an extended mission is planned, during which any regions within ISS latitude constraints could be targeted.

In this study, we present the first results using EMIT to characterize methane and carbon dioxide point sources from the first 30 days of data collection. We generated methane and carbon dioxide retrievals using EMIT radiance data; estimated emission rates using the integrated mass enhancement (IME) combined with wind speeds; and attributed emissions to the oil and gas, waste, and energy sectors. We focused our analysis on a number of countries in the Middle East and Central Asia with considerable production of oil, gas, and coal and limited emissions reporting. We present the overall distribution of observed emissions to assess its potential for improving our understanding of global greenhouse gas budgets and to inform mitigation strategies.

RESULTS

EMIT coverage, revisit frequency, and implications for emission estimates

Given a primary mission to map the mineral composition of arid lands, EMIT targets the white regions shown in Fig. 1A, an area of 2.8×10^7 km^2 and 19.3% of Earth′s land surfaces. In the first 30 days of data collection, EMIT′s total coverage was 3.8×10^7 km^2. This includes regions with methane emissions as predicted by bottom-up inventories like those of Scarpelli *et al.* (*56*), particularly for the Western United States, North and West Africa, the Middle East, and Central and East Asia, as well as a number of power plants from Annex I and Non–Annex I countries (Fig. 1A). EMIT′s wide coverage offers the potential for identifying emissions not only in regions where we might anticipate emissions but also in places where there is poor prior knowledge of emissions.

Figure 1B shows the expected distribution of the EMIT revisit rate over the course of its 1-year primary mission. This simulation does not include all calibration targets, cloud cover screened out on board, or potential downlink interruptions. However, the simulation gives a sense of the typical revisit capability of the instrument, with a median of 10 revisits per annum and 90% of the target mask having between 3 and 15 revisits. If revisits were evenly spaced, then this is equivalent to a median average revisit rate of 36.5 days (90% of the target mask with a frequency between 24 and 122 days), although the revisit interval is rarely even due to a combination of ISS trajectory and solar angles. Some locations near the +51.6° and −51.6° turning points of the ISS orbit will receive more than 20 revisits over the year, with a minimum average revisit interval of 4.9 days. The precessing ISS orbit allows for sampling across the sunlit interval, thus allowing assessment of diurnal variability for some emission sources. This unique combination of large area coverage and repeat measurements enables tracking of emissions over time, an assessment of persistence, and reduction in uncertainties associated with carbon budgets.

Mapping and attributing carbon dioxide and methane emissions

We demonstrate the capability of EMIT for quantifying poorly characterized emissions from carbon dioxide and methane point sources and attributing collocated emissions to distinct emission sectors. Both of these capabilities are critical to resolving a class of highly uncertain emissions occurring at fine spatial scales that constitute an important source of uncertainty in the global carbon budget. Cusworth *et al.* (*46*) demonstrated the quantification of carbon dioxide plumes using both the airborne GAO and spaceborne PRISMA imaging spectrometers with good agreement against reported emissions for U.S. power plants. This highlights the potential for quantifying carbon dioxide emissions from global stationary sources using instruments such as EMIT, which is

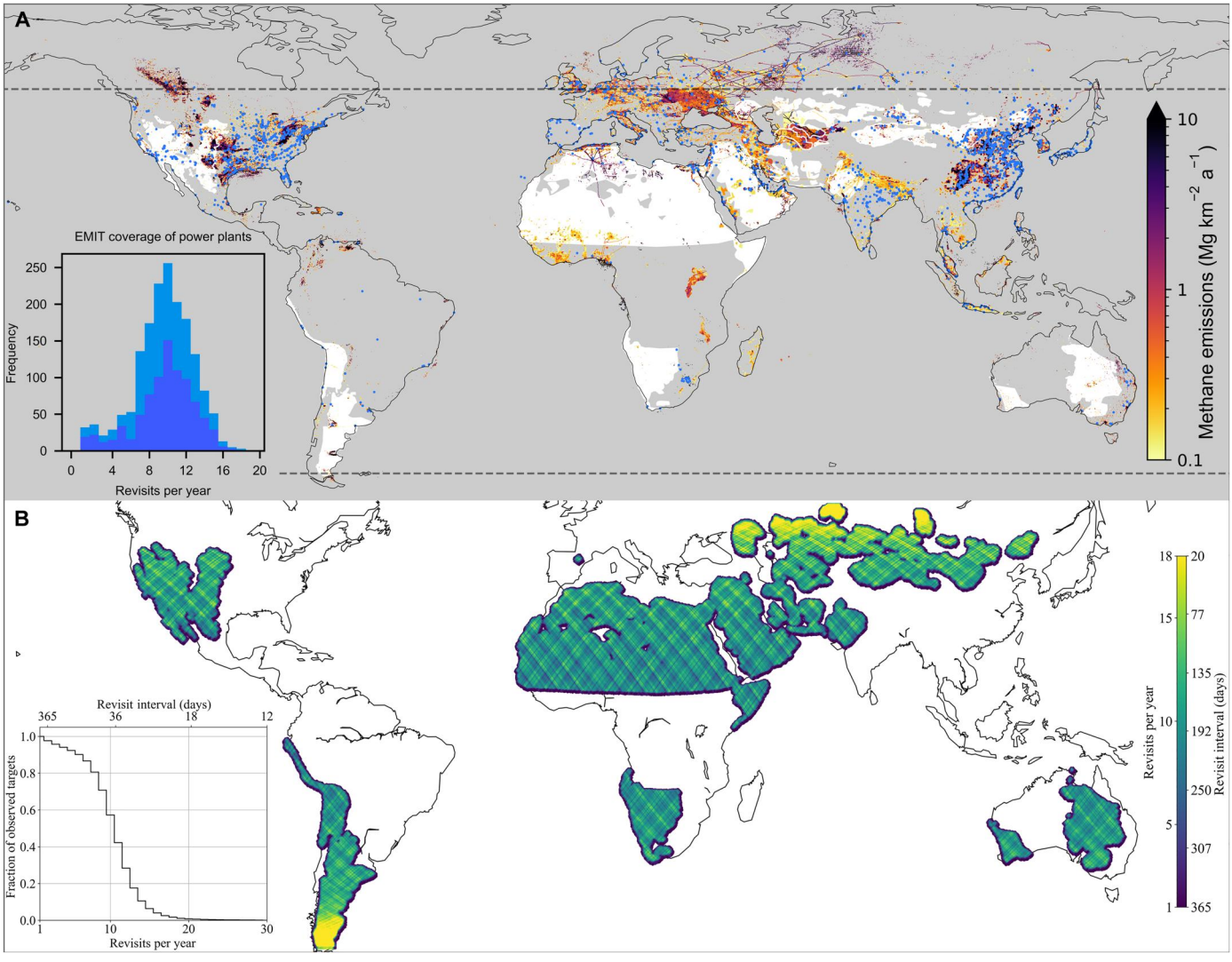

Fig. 1. EMIT coverage and total observations for simulated 1-year mission. (**A**) EMIT observation mask shown in white relative to bottom-up methane inventory (*56*) and locations of power plants with ≥500-MW capacity shown in blue (*58*). The inlay stacked histogram shows ≥500-MW power plants that will be observed with EMIT and associated revisits for the 1-year primary mission for non–Annex I (dark blue) and Annex I (light blue) countries. EMIT should complete its primary mission by September 2023, and in the planned extended mission, any terrestrial region between the dashed lines (+51.6° and −51.6° latitude) could be targeted. (**B**) Total observations and average revisit interval for nominal 1-year mission.

particularly important for non–Annex I countries where emissions are not reported and uncertainties remain high.

Repeat observations of power plants are critical to constrain annual facility emissions in jurisdictions that lack continuous emission monitoring and reporting. Hill *et al.* (*57*) estimated that 18 OCO-2 observations are needed to constrain annual carbon dioxide emissions of fossil fuel power plants to within 15%, while 29 PRISMA overpasses are required to reduce non–Annex I fossil fuel power plant emission uncertainty below 1 Gt CO_2 per year (within 14%) (*46*). Figure 1A shows the locations of power plants with ≥500-MW capacity (*58*), and the inlay shows the distribution of those power plants that will be observed with EMIT during the 1-year primary mission. Measurements range from 1 to 18 revisits for 856 non–Annex I and 828 Annex I power plants with approximately half observed ≥10 times. Given this, EMIT observations will contribute appreciably to the observational requirements needed to constrain stationary source carbon dioxide emissions.

Carbon dioxide plumes for two coal-fired power plants in the Xinjiang Uygur Autonomous Region of the People's Republic of China are shown in Fig. 2A. Carbon dioxide emissions were estimated at 1571 ± 229 tonnes CO_2 hour^{-1} for the Shenhuo Zhundong (1400-MW capacity) and 3511 ± 537 tonnes CO_2 hour^{-1} for the Xinjiang Qiya Smelter (2160-MW capacity) power stations (*59*). In both examples, the observed plumes are collocated with combustion stacks. While these power plants lack continuous emission monitoring and reporting, EMIT will provide 13 repeat observations during the 1-year primary mission, offering the potential to better constrain emissions at these two facilities.

Decomposition of organic material in anaerobic conditions results in considerable waste sector methane emissions,

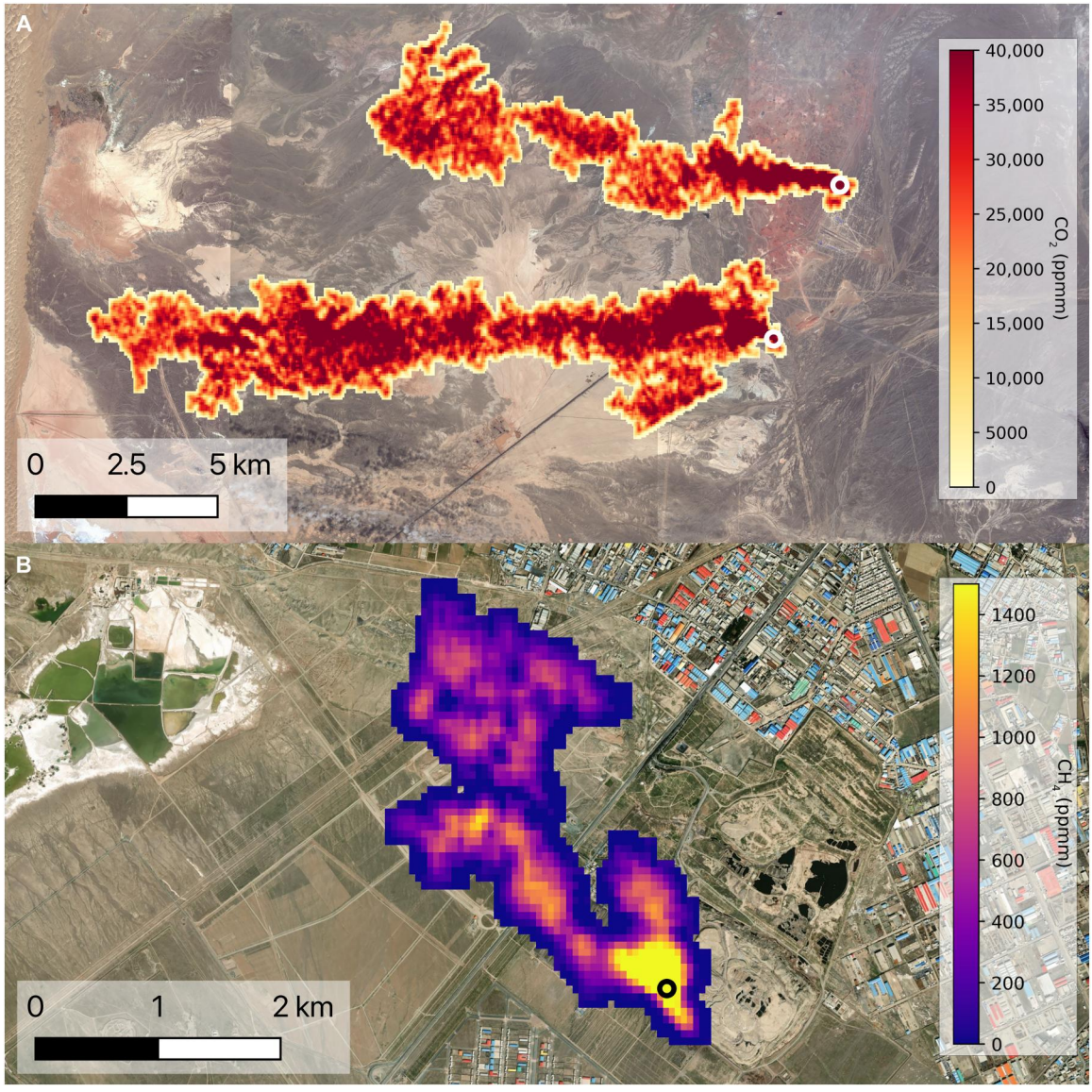

Fig. 2. Carbon dioxide plumes from power plants and methane from landfill observed from space. (**A**) Carbon dioxide plumes from emission stacks at two power plants in China (1571 ± 229 tonnes CO_2 hour^{-1} example to the north; 3511 ± 537 tonnes CO_2 hour^{-1} example to the south). (**B**) Methane plume from active face of a landfill in Iran (5 ± 1 tonnes CH_4 hour^{-1}). ppmm, parts per million meter.

representing around 18% (for solid waste and wastewater) of global anthropogenic methane emissions (*8*). Largely driven by population growth (*60*), global solid waste sector emissions are expected to double by 2050 with uncertainties remaining high (*61*). Recent studies have identified large methane emissions at landfills and waste dumps in the United States (*35*, *39*), Argentina, and India (*18*). While a complete global database of landfills and dumps currently does not exist, satellite observations have the potential to play an important role in landfill geolocation and methane emission monitoring.

Methane emissions were observed for 11 landfills in this study. One example is shown in Fig. 2B, where a methane plume is clearly visible (5 ± 1 tonnes CH_4 hour^{-1}) and is consistent with emissions from the active face of the Arad Kouh landfill near Tehran, Iran. Operating since 1976, this facility uses sorting and recycling of waste, as well as composting (*62*), but does not use a landfill gas capture system.

Figure 3 highlights EMIT′s ability to pinpoint multiple emission sources that are in close proximity and to attribute these emissions to different sectors. Methane plumes appear from multiple sources including the Riyadh landfill in Saudi Arabia (8 ± 2 tonnes CH_4 hour^{-1}). Opened in 2006, this landfill receives unsorted waste and uses an open collection pit for leachate (*63*). A methane plume also appears from a sewage treatment plant (7 ± 1 tonnes CH_4 hour^{-1}) and natural gas–fired power plant (30 ± 2 tonnes CH_4 hour^{-1}) (*64*), where a carbon dioxide plume was also visible (2032 ± 142 tonnes CO_2 hour^{-1}). Emissions of methane likely associated with power plant startup conditions have been quantified in previous studies using airborne in situ (*65*, *66*) and imaging spectrometer measurements (*67*). Given the overlap between methane plumes,

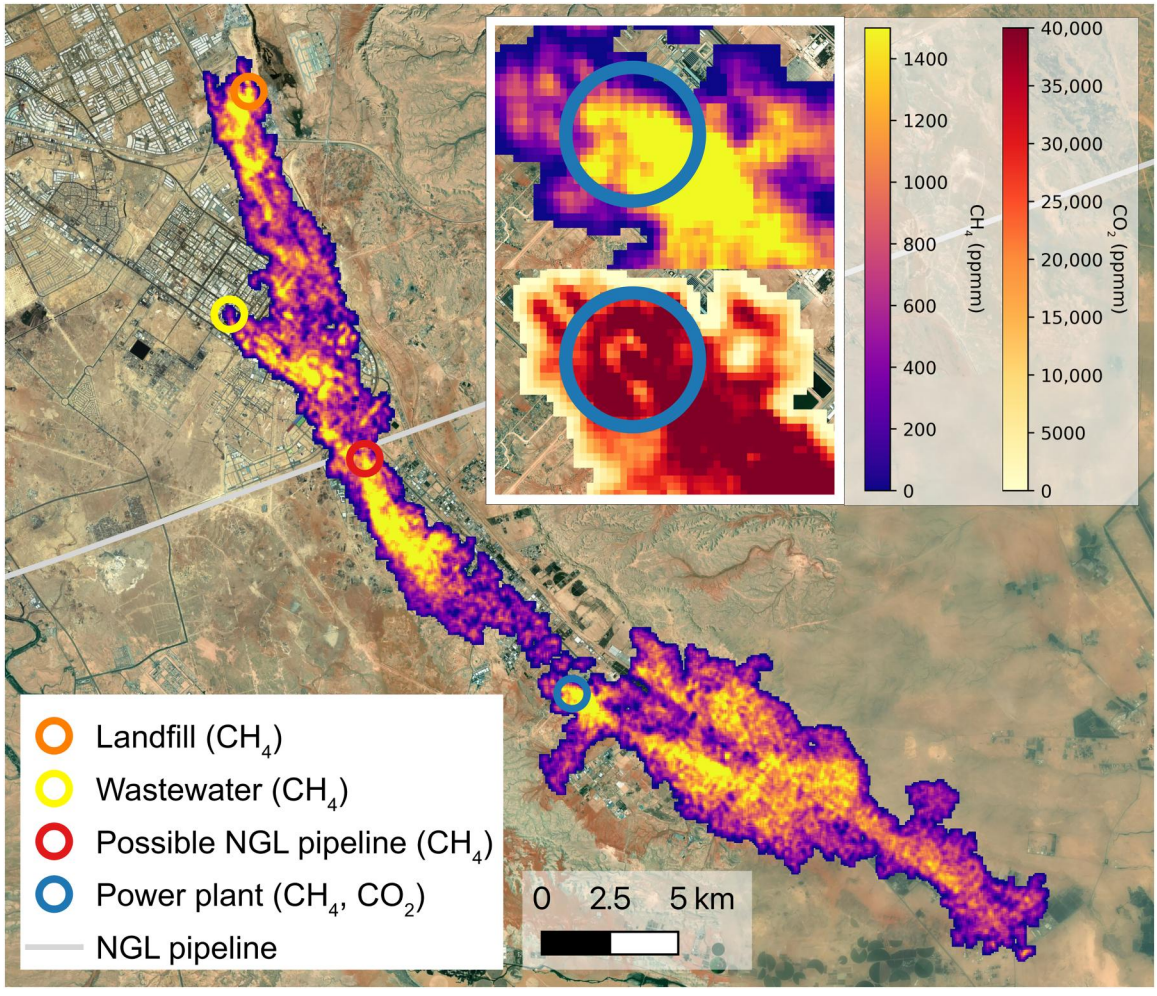

Fig. 3. Source attribution of greenhouse gas plumes in close proximity from different emission sectors. Emissions from a landfill in Saudi Arabia (28 ± 2 tonnes CH_4 hour^{-1}), from a wastewater treatment facility (7 ± 1 tonnes CH_4 hour^{-1}), from a power plant (30 ± 2 tonnes CH_4 hour^{-1} and 2032 ± 142 tonnes CO_2 hour^{-1}), and potentially from a natural gas pipeline (28 ± 2 tonnes CH_4 hour^{-1}). Inlay images show a close up of the power plant source, with colocated methane and carbon dioxide emissions. NGL, natural gas liquids.

interpretation of additional sources is challenging; however, a potential source (28 ± 2 tonnes CH_4 hour^{-1}) was identified in close proximity to the Shedgum-Yanbu natural gas liquids pipeline (*68*).

Multiple prominent methane plumes were observed in Turkmenistan near the Caspian Sea, including a set of 12 sources shown in Fig. 4A, with total emissions of 163 ± 18 tonnes CH_4 hour^{-1}. Clusters of plumes are associated with the Goturdepe and the Barsagelmez fields, both producing crude oil, condensate, and natural gas liquids (*69*). Oil and gas pipelines are also shown; however, all emission sources appear associated with gathering lines that are visible in high-resolution imagery available on Google Earth. This location was imaged twice on 15 August 2022 at 4:28 UTC (54° solar zenith) and 10:58 UTC (38° solar zenith), and the orientation of the methane plumes changes with shifting wind direction (Fig. 4A, inset). The ISS precessing orbit enables this unique capability to assess emission variability at two times throughout the day. In Fig. 4B, another set of 15 methane plumes was observed at the Dauletabad-Donmez field (condensate, natural gas liquids, and gas), with sources that include a gas compressor station, flares, and gathering lines. For this example, total emissions were estimated at 64 ± 12 tonnes CH_4 hour^{-1}. A number of methane sources shown in Fig. 4 were located in close proximity, which resulted in overlap for those areas used to estimate IME values with the prescribed 1000-m maximum fetch (see the "Calculating emissions" section). In these examples, overlapping plumes were removed to ensure that emissions were not overestimated.

Methane emissions from the Middle East and Central Asia

We analyzed emissions from energy-producing countries in the Middle East (Saudi Arabia, Iran, the United Arab Emirates, Iraq, Qatar, Kuwait, and Oman) and Central Asia (Kazakhstan, Turkmenistan, and Uzbekistan). These countries have large disagreement between global inversion results (*70*, *71*) and discrepancies relative to bottom-up inventories (*56*). Figure 5 shows coverage by country for data acquired in the first 30 days of the EMIT mission, as well as the location, magnitude, and sector for observed plumes.

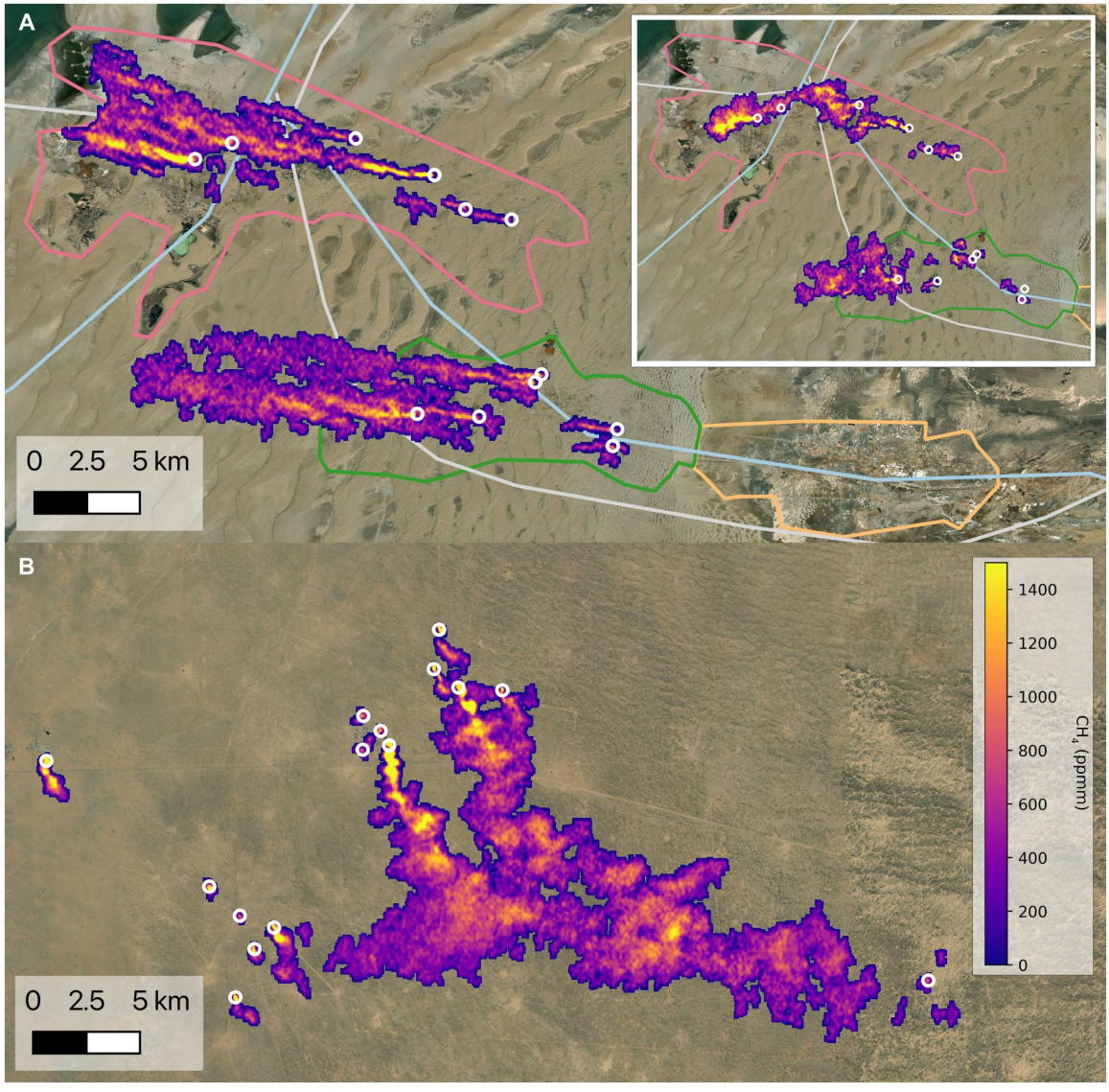

Fig. 4. Clusters of methane plumes in Turkmenistan with distinct sources. (**A**) Twelve methane sources with an aggregate emission of 163 ± 18 tonnes CH_4 $hour^{-1}$ acquired at 4:28 UTC on 15 August 2022. The inlay shows a repeat mapping of this region on the same day (10:58 UTC) with visible differences in the plume shapes associated with changing wind conditions. Infrastructure locations are shown for the Goturdepe (pink), Barsagelmez (green), and Burun (orange) fields, as well as gas (light gray) and oil (light blue) pipelines. (**B**) Fifteen sources all within the Dauletabad-Donmez field, with an aggregate emission of 64 ± 12 tonnes CH_4 $hour^{-1}$.

The spatial distribution of the oil and gas methane emissions shown in Fig. 5 clearly indicates significant regional differences. For example, Saudi Arabia is the world's largest oil exporter; however, we identified only one methane plume from the Saudi oil and gas sector with EMIT despite covering 65% of the country. The total number and magnitude of observed oil and gas emissions from Turkmenistan are far greater than its neighboring countries, Iran and Uzbekistan, but the root causes for these differences are unclear. Uzbekistan and Turkmenistan production is mostly from natural gas (90 and 87%, respectively) (*72*); however, their oil and gas emissions differed markedly (87 ± 22 and 731 ± 148 tonnes CH_4 $hour^{-1}$, respectively).

While there are considerable uncertainties associated with global methane flux inversion results attributed to these countries, Turkmenistan, Uzbekistan, and Iran have consistently appeared as the largest methane emitters in the region (*70*, *71*). Using TROPOMI results, Lauvaux *et al.* (*73*) identified Turkmenistan, Iran, and Kazakhstan as the largest methane emitters in Central Asia. Consistent with these prior studies, EMIT results indicate that Turkmenistan (731 ± 148 tonnes CH_4 $hour^{-1}$), Kazakhstan (207 ± 11 tonnes CH_4 $hour^{-1}$), Iran (87 ± 48 tonnes CH_4 $hour^{-1}$), and Uzbekistan (86 ± 22 tonnes CH_4 $hour^{-1}$) represent the largest oil and gas emitters of those countries analyzed in this study. While these initial EMIT results are promising, future analyses will use additional observations to ensure that these countries are mapped in their entirety and revisited to determine emission persistence.

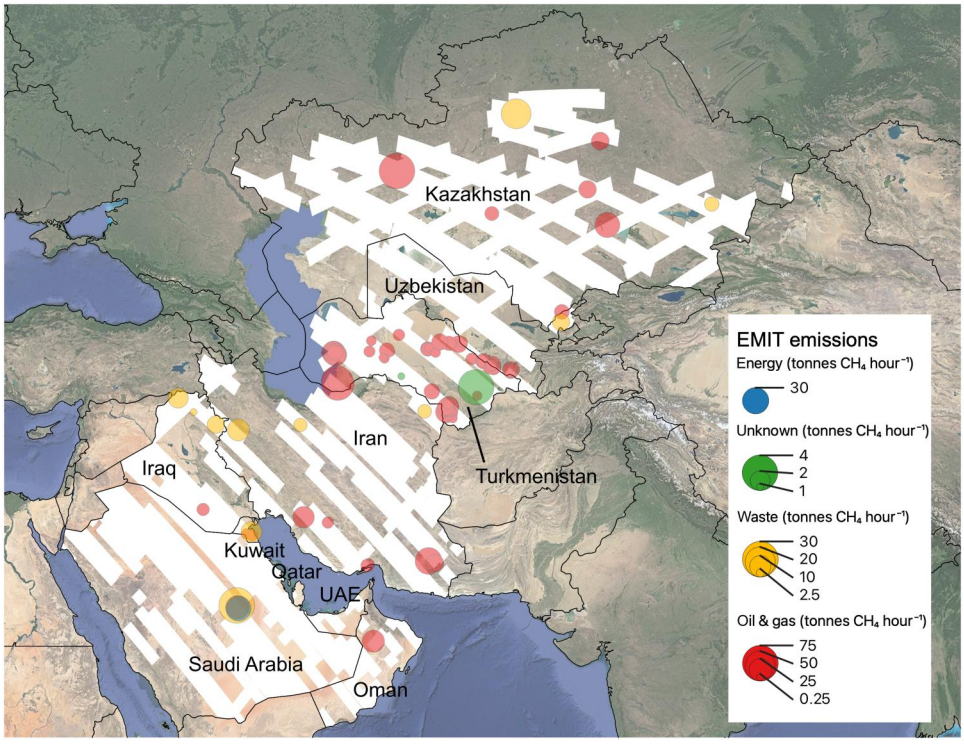

Fig. 5. Location, magnitude, and emission sector for methane plumes observed in the Middle East and Central Asia. Distribution of methane emissions for selected countries in the Middle East and Central Asia with considerable production of oil, gas, and coal. The magnitude of observed emissions is shown for the oil and gas, waste, and energy sectors (emission magnitude associated with circle size varies by sector). EMIT cloud-free acquisitions are shown in white.

Previous studies identified a handful of large methane sources in Turkmenistan using GHGSat (*16*), Sentinel 2 (*21*), and Worldview (*23*). Lauvaux *et al.* (*73*) identified 118 point sources, mostly above 10 tonnes CH_4 $hour^{-1}$ and associated with oil and gas activity in Turkmenistan using TROPOMI and its 5.5 km–by–7 km spatial resolution. While Irakulis-Loitxate *et al.* (*74*) used PRISMA to quantify methane emissions for oil and gas fields near the Caspian Sea, EMIT imaged 64% of Turkmenistan in just its first 30 days of data collection. From this initial survey, we identified 65 emission sources almost entirely from the oil and gas sector, ranging from 0.3 to 60 tonnes CH_4 $hour^{-1}$, that were attributed to specific source locations and organized by upstream (well pad and gathering line), midstream (gas compressor stations and gas processing plant), and downstream (fertilizer plant) categories.

The distribution of methane emission rates observed by EMIT in its first 30 days (0.3 to 73 tonnes CH_4 $hour^{-1}$) is shown in Fig. 6A for the regions identified in Fig. 5A. Compared to airborne results (AVIRIS-NG and GAO) across a number of regions in the United States, the EMIT distribution is shifted to larger emissions. This is expected both because EMIT is observing a class of emissions far larger than those seen in U.S. airborne surveys and because EMIT is less sensitive to smaller emission rates due to the coarser spatial resolution. However, there is substantial overlap in observed emissions. For example, the lowest emission observed with EMIT was 0.3 tonnes CH_4 $hour^{-1}$, and emissions greater than this value represent 60 to 85% of the total emissions measured with the airborne surveys.

The total EMIT detected emissions by sector is shown in Fig. 6B, with 88.7% from oil and gas (63.5% upstream, 24.3% midstream, and 0.9% downstream). Emissions from the waste sector represent 8.6% of total observed emissions, including examples from 11 landfills and one wastewater treatment facility (Fig. 2C). For this study, the landfill emissions ranged from 2 to 28 tonnes CH_4 $hour^{-1}$, which is broadly consistent with previous studies that showed estimates from four landfills in Argentina and India that ranged from 3 to 29 tonnes CH_4 $hour^{-1}$. We note that the emission sources detected were serendipitously within the EMIT observation mask. More complete statistics for those regions will become available as more data is evaluated and other locations can be targeted during the EMIT extended mission.

DISCUSSION

EMIT provides important contributions through the combination of large area coverage and fine spatial resolution imaging spectroscopy data, enabling potential future identification of both expected (process-based) and unexpected (fugitive) emissions. Emissions can be quantified and attributed to specific sectors, which is particularly important when multiple emissions from different sectors are present in close proximity (Fig. 3). We highlight the first examples of EMIT imaging spectrometer observations of methane and carbon dioxide emissions from sources spanning the oil and gas (upstream, midstream, and downstream), waste (landfill and wastewater treatment), and energy sectors (power plant).

We focused our analysis on a number of energy-producing countries in the Middle East (Saudi Arabia, Iran, the United Arab Emirates, Iraq, Qatar, Kuwait, and Oman) and Central Asia (Kazakhstan, Turkmenistan, and Uzbekistan). Oil and gas methane emissions represented 88.7% of the total (63.5% upstream, 24.3%

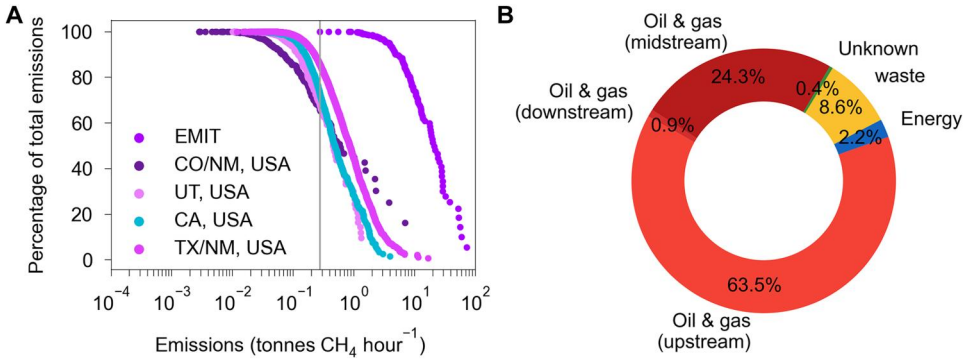

Fig. 6. Distribution of methane emissions observed with EMIT relative to previous studies. (**A**) Heavy-tailed distribution of methane emissions for results shown in Fig. 5 (Middle East and Central Asia) from EMIT compared to previous airborne campaign results made available through the Carbon Mapper open data portal (data.carbonmapper.org). The vertical gray line indicates the smallest EMIT emission (0.3 tonnes CH_4 $hour^{-1}$) observed in this study and emissions greater than this value represent 60 to 85% of the total emissions measured with the airborne surveys. (**B**) EMIT emissions by sector as determined from the first 30 days of data collection.

midstream, and 0.9% downstream), followed by waste (8.6%) and energy (2.2%). Turkmenistan, Kazakhstan, Iran, and Uzbekistan represent the largest emitters of those countries analyzed in this study, consistent with previous studies (*70*, *71*).

This study provides a 30-day snapshot of multinational methane emissions, and the initial set of EMIT observations did not provide 100% spatial coverage of individual counties or the repeat mapping required to assess persistence. Despite these limitations, initial results from EMIT indicate considerable variability in methane emissions at the regional and country scales while providing insights into regions with relatively large emissions and incomplete activity reporting. Additional observations with an average 50-day repeat frequency will permit assessment over time to determine emission persistence and reduce uncertainty in global greenhouse gas budgets. During the 1-year primary mission, more than 1600 power plants (≥500-MW capacity) will be imaged by EMIT with approximately half observed ≥10 times. In some cases, the ISS orbit enables the additional unique capability of assessing emission variability two times throughout the day. In September 2023, EMIT should complete its primary mission, and an extended mission is planned, during which any regions within ISS latitude constraints could be targeted.

Emissions observed by EMIT from individual plumes ranged between 0.3 and 73 tonnes CH_4 $hour^{-1}$, and the 11 landfill examples presented here had emissions between 2 and 28 tonnes CH_4 $hour^{-1}$. The smallest emission observed in this study was 0.3 tonnes CH_4 $hour^{-1}$, and emissions greater than this value represent 60 to 85% of the total emissions measured with the airborne surveys in the United States. This emphasizes the potential of EMIT to map large regions that are difficult to access with airborne surveys. Analysis of additional observations are required to determine EMIT's detection limit for methane and carbon dioxide point sources, which has important implications for understanding what emissions remain undetected relative to total emissions. Nevertheless, EMIT is almost two orders of magnitude more sensitive than TROPOMI (minimum detection limit of 10 tonnes CH_4 $hour^{-1}$), enabling myriad future studies. In addition, we demonstrated EMIT's ability to identify, geolocate, and quantify multiple emission sources (methane and/or carbon dioxide) that are in close proximity (<1 km) and to attribute these emissions to different sectors. These capabilities, enabled by the 60-m spatial resolution, are needed to close carbon budgets.

Building on the design heritage and capabilities of the EMIT instrument, the JPL as part of the Carbon Mapper Coalition is supporting the launch of the first two satellites equipped with a JPL-developed imaging spectrometer in late 2023. Those instruments will feature an improved 5-nm spectral sampling and finer spatial resolution (30 m) and will be hosted on Planet Labs' satellites, offering target tracking (higher effective SNR) in noon-crossing sun-synchronous orbits, resulting in greater sensitivity for methane and carbon dioxide point source emissions. Combining measurements obtained from different instruments improves global coverage and revisit frequency, which is critical to improving understanding of global emissions and informing mitigation strategies. To this end, the EMIT greenhouse gas applications online mapping tool (https://earth.jpl.nasa.gov/data/data-portal/Greenhouse-Gases) will facilitate the distribution of scientific findings in support of NASA's Open Source Science Initiative.

MATERIALS AND METHODS

EMIT imaging spectrometer

The EMIT is an imaging spectrometer that measures reflected solar radiation for 285 distinct wavelengths from the visible to shortwave infrared (381 to 2493 nm) (*25*, *26*). This pushbroom instrument builds on the 30-year history of imaging spectrometer development at the JPL and uses a large concave-shaped blaze grating fabricated at the JPL Microdevices Laboratory and a CHROMA (Teledyne Imaging Sensors Inc.) HgCdTe detector. Its Dyson optical design enables spatial uniformity exceeding 98%, and an F number of 1.8. EMIT has demonstrated exceptionally high optical throughput performance, with a spectral uniformity greater than 98% (less than 0.2-nm peak-to-peak or 0.1-nm peak-to-center smile) and an SNR ranging from 500 to 750 for most wavelengths at the USGS Libya 4 calibration site (*55*). While designed to determine the mineral composition of arid lands responsible for dust generation, the greenhouse gas mapping capability has been demonstrated using airborne imaging spectrometers built at JPL (*28*–*30*, *33*–*40*, *42*–*46*).

EMIT uses a 1242-pixel element swath at approximately 60-m image pixel resolution, resulting in an image swath around 80 km with an average daily coverage of 1.3×10^6 km^2. While the primary

mission is focused on coverage of arid lands, EMIT will map broad regions of Earth's surface between +51.6° and −51.6° latitude (Fig. 1A), which is dictated by the inclined, equatorial orbit of the ISS. The ISS orbit coupled with the large daily coverage, equivalent to an area the size of the Republic of South Africa, results in a median revisit frequency of 36.5 days. This offers the potential to track changes in emissions over time (Fig. 1B), and in rare cases, multiple observations can be obtained within the same day (Fig. 4A).

Methane and carbon dioxide retrievals

Greenhouse gas retrievals using airborne imaging spectrometers were first demonstrated with AVIRIS (*75*) and AVIRIS-NG (*45*). These algorithms use absorption spectroscopy in the shortwave infrared to retrieve gas concentrations from solar backscatter radiance for each image pixel within a scene. At the 7.4-nm EMIT spectral sampling, methane and carbon dioxide have distinct spectral fingerprints, as shown in fig. S1. In this study, we use a linearized matched filter to calculate a mixing ratio length in units of ppmm (parts per million meter), representing the thickness and concentration within a volume of equivalent absorption (*76*). This retrieval has been demonstrated on both airborne (*33*–*40*) and spaceborne data (*15*). We used radiative transfer simulations to generate unit absorption spectra (*38*) for methane and carbon dioxide parameterized for each EMIT scene (path length, viewing geometry, and atmospheric water vapor modeled by the primary EMIT mission), which are used to convert changes in radiance associated with gas absorptions in the units of parts per million meter. Methane and carbon dioxide retrieval results were used to generate the plume imagery presented here and for emission attribution and quantification described below.

Calculating emissions

Emission estimates are generated by combining the IME, plume length, and wind speed as described in previous studies (*40*). The IME was calculated by applying a mixing ratio threshold to separate the plumes from background (500 ppmm for methane and 25,000 ppmm for carbon dioxide). The plume was then delineated using a merge distance defined in meters to isolate contiguous plume elements in the presence of gaps (pixels with low methane or carbon dioxide values) and a maximum plume fetch (radius in meters from the plume origin). Higher mixing ratio thresholds and lower merge distances typically result in plumes that are well defined and contiguous but have shorter plume lengths. An iterative assessment of these parameters, balancing the need for clear delineation of plumes but limiting the amount of overlap between plumes that are located in close proximity (Fig. 4), resulted in a 200-m merge distance and 1000-m maximum fetch. For the plumes in this study, the average plume length used for the emission calculation was 861 m (163-m SD).

The IME is calculated as follows

$$\mathrm{IME} = k\sum_{i=0}^{n}\alpha(i)S(i) \quad (1)$$

by summing the product of α (the mixing ratio length in units of ppmm methane or carbon dioxide) multiplied by the pixel area S (in m^2) for the n pixels in the plume and then converting to methane or carbon dioxide mass units using a constant k. The IME (tonnes of methane or carbon dioxide) is combined with L, the plume length (in m), and 10-m above surface wind speed (in m s^{-1}) to estimate the emission rate (in tonnes $hour^{-1}$) using the following equation

$$Q = \frac{\mathrm{IME}\ \overline{U}_{10}}{L} \quad (2)$$

Wind speed information was obtained using the ECMWF ERA5 hourly data (*77*). Using the UTC timestamp associated with the acquisition for a given EMIT scene coupled with the latitude and longitude of the plume origin, 10-m u and v components were used to calculate a mean ($\overline{U}_{10}$) and SD (σ_U) wind speed (in m s^{-1}) for nine grid cells (3 × 3 box) centered on the plume origin. The mean 10-m wind speed ($\overline{U}_{10}$) was used in the equation above, while the uncertainty in the emissions were calculated using the SD (σ_U) of the winds. For emissions presented in this study, $\overline{U}_{10}$ ranged from 0.9 to 9.5 m s^{-1} (4.3 m s^{-1} mean; 1.9 m s^{-1} for 1σ) and winds associated with the lowest and highest emission estimates were 3.9 and 6.3 m s^{-1}. Using AVIRIS-NG, emission estimates derived from the IME, plume length, and wind speed have been validated through comparison with independent estimates obtained using mass balance approaches from in situ gas sampling (*30*, *40*) and controlled release experiments (*78*).

The choice of mixing ratio thresholds and maximum plume fetch will affect the IME/L component of Eq. 2 and, ultimately, the emission rate. In Fig. 7A, the IME/L values shown on the x axis represent those presented in this study (500-ppmm mixing ratio threshold and 1000-m maximum fetch) and those in y axis use 500-m maximum fetch. The use of the smaller 500-m maximum fetch typically results in higher IME/L values. In Fig. 7B, results that are shown on the x axis represent those presented in this study and those in the y axis use a 750-ppmm mixing ratio threshold, indicating that IME/L values for the 750-ppmm mixing ratio threshold are slightly lower. IME/L values calculated for different CH_4 mixing ratio threshold and maximum plume fetch for CH_4 plumes are also plotted in Fig. 8. Outlier values tend to be associated with the smaller 500-m maximum fetch (green and orange circles), and the IME/L values using the 500-ppmm mixing ratio threshold

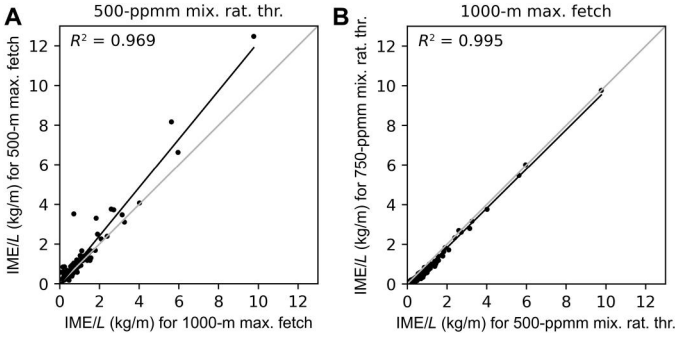

Fig. 7. IME/*L* values calculated for different CH_4 mixing ratio threshold and maximum plume fetch. (**A**) Results shown on the *x* axis represent those presented in this study using 500-ppmm mixing ratio threshold and 1000-m maximum fetch and those on the *y* axis using 500-m maximum fetch. The use of the smaller 500-m maximum fetch typically results in higher IME/*L* values. (**B**) Results shown on the *x* axis represent those presented in this study using 500-ppmm mixing ratio threshold and 1000-m maximum fetch and those on the *y* axis using 750-ppmm mixing ratio threshold.

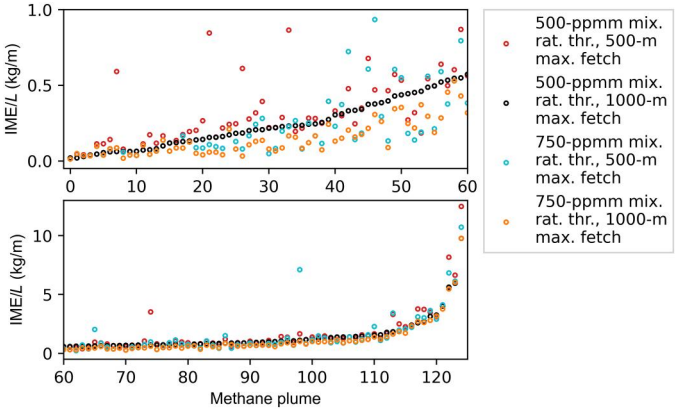

Fig. 8. Sorted IME/*L* values calculated for different CH_4 mixing ratio threshold and maximum plume fetch for CH_4 plumes presented in this study. High outlier values tend to be associated with the smaller 500-m maximum fetch (red and blue circles). IME/*L* values presented in this study (black circles) were generated using the 500-ppmm mixing ratio threshold, and 1000-m maximum fetch were, in most, cases bounded by the IME/*L* values calculated using different combinations of mixing ratio threshold and maximum fetch.

and 1000-m maximum fetch were, in most cases, bounded by the IME/*L* values calculated using different combinations of mixing ratio threshold and maximum fetch (Fig. 8, black circles). However, results diverged for larger IME/*L* values.

The use of the 1000-m maximum fetch ensured that we used the portion of the plume closest to the ground. Given this, we used the 10-m *u* and *v* ECMWF ERA5 wind components rather than the 100-m *u* and *v* components. Future work will focus on exploring additional emission estimation approaches, including the use of the effective wind speed that accounts for turbulent diffusion and faster transport aloft (*79*) and opportunities to compare estimated emission from EMIT to known emissions as part of controlled release experiments (*80*).

Emissions were calculated for each plume, and the results were compared to previous airborne campaigns (Fig. 6). If multiple plumes were located in close proximity (Fig. 4) and there was overlap for those areas used to estimate IME values, then the overlapping examples were removed to ensure that emissions were not overestimated. For rare examples where there were multiple observations of the same source (Fig. 4A), an average emission rate was estimated to avoid double counting of emissions, and these results were used in Fig. 5.

Identification and attribution of emissions

Image analysts systematically examined entire methane and carbon dioxide retrievals to identify all candidate gas plumes within each scene. Scenes with heavy cloud cover were flagged and excluded from the EMIT coverage mask shown in Fig. 5. For each plume, an initial assessment of the plume origin was made on the basis of plume morphology and the distribution of concentrations present in a scene. Candidate gas plumes were subsequently assessed a second time to ensure that only high-confidence examples were included in this study.

EMIT generates true color images at 60-m spatial resolution, but in most cases, imagery at this resolution is insufficient to attribute plumes to specific emission sectors and infrastructure types. For attribution, we relied on high-resolution imagery provided through Google Earth that was co-registered with EMIT true color imagery and methane and carbon dioxide maps. Emissions were assigned to broad sector and subsector categories, including waste (landfill and wastewater treatment), energy (power plant), and oil and gas (upstream, midstream, and downstream). Upstream was defined as infrastructure associated with production (well pad and gathering line). Midstream was associated with processing, storage, and transport (gas compressor station and gas processing plant), and downstream was associated with refining, purifying, and distribution (refinery and fertilizer plant). Two methane sources that could not be confidently attributed are shown in Figs. 5 and 6 in the unknown category.

EMIT data availability

All EMIT radiance data are available through the Land Processes Distributed Active Archive Center (LP DAAC) at the following link: https://lpdaac.usgs.gov/products/emitl1bradv001. All codes are available at https://doi.org/10.5281/zenodo.8156665 (*81*), https://github.com/emit-sds, and https://github.com/emit-sds/emit-ghg. The plume examples presented in this study are available through the EMIT greenhouse gas applications online mapping tool (https://earth.jpl.nasa.gov/emit/data/data-portal/Greenhouse-Gases/) developed using the Multi-Mission Geographic Information System (MMGIS) (*82*). This tool will facilitate the distribution of scientific findings in support of NASA's Open Source Science Initiative, including EMIT coverage to date, forecasted acquisitions, mission objectives such as mineralogy, and EMIT applications such as greenhouse gas mapping.

Supplementary Materials

This PDF file includes:

Text S1 and S2
Fig. S1
Table S1

REFERENCES AND NOTES

1. P. Friedlingstein, M. W. Jones, M. O'Sullivan, R. M. Andrew, D. C. E. Bakker, J. Hauck, C. Le Quéré, G. P. Peters, W. Peters, J. Pongratz, S. Sitch, J. G. Canadell, P. Ciais, R. B. Jackson, S. R. Alin, P. Anthoni, N. R. Bates, M. Becker, N. Bellouin, L. Bopp, T. T. T. Chau, F. Chevallier, L. P. Chini, M. Cronin, K. I. Currie, B. Decharme, L. M. Djeutchouang, X. Dou, W. Evans, R. A. Feely, L. Feng, T. Gasser, D. Gilfillan, T. Gkritzalis, G. Grassi, L. Gregor, N. Gruber, Ö. Gürses, I. Harris, R. A. Houghton, G. C. Hurtt, Y. Iida, T. Ilyina, I. T. Luijkx, A. Jain, S. D. Jones, E. Kato, D. Kennedy, K. Klein Goldewijk, J. Knauer, J. I. Korsbakken, A. Körtzinger, P. Landschützer, S. K. Lauvset, N. Lefèvre, S. Lienert, J. Liu, G. Marland, P. C. McGuire, J. R. Melton, D. R. Munro, J. E. M. S. Nabel, S.-I. Nakaoka, Y. Niwa, T. Ono, D. Pierrot, B. Poulter, G. Rehder, L. Resplandy, E. Robertson, C. Rödenbeck, T. M. Rosan, J. Schwinger, C. Schwingshackl, R. Séférian, A. J. Sutton, C. Sweeney, T. Tanhua, P. P. Tans, H. Tian, B. Tilbrook, F. Tubiello, G. R. van der Werf, N. Vuichard, C. Wada, R. Wanninkhof, A. J. Watson, D. Willis, A. J. Wiltshire, W. Yuan, C. Yue, X. Yue, S. Zaehle, J. Zeng, Global Carbon Budget 2021. *Earth Syst. Sci. Data* **14**, 1917–2005 (2022).
2. P. Friedlingstein, M. O'Sullivan, M. W. Jones, R. M. Andrew, J. Hauck, A. Olsen, G. P. Peters, W. Peters, J. Pongratz, S. Sitch, C. L. Quéré, J. G. Canadell, P. Ciais, R. B. Jackson, S. Alin, L. E. O. C. Aragão, A. Arneth, V. Arora, N. R. Bates, M. Becker, A. Benoit-Cattin, H. C. Bittig, L. Bopp, S. Bultan, N. Chandra, F. Chevallier, L. P. Chini, W. Evans, L. Florentie, P. M. Forster, T. Gasser, M. Gehlen, D. Gilfillan, T. Gkritzalis, L. Gregor, N. Gruber, I. Harris, K. Hartung, V. Haverd, R. A. Houghton, T. Ilyina, A. K. Jain, E. Joetzjer, K. Kadono, E. Kato, V. Kitidis, J. I. Korsbakken, P. Landschützer, N. Lefèvre, A. Lenton, S. Lienert, Z. Liu, D. Lombardozzi, G. Marland, N. Metzl, D. R. Munro, J. E. M. S. Nabel, S. I. Nakaoka, Y. Niwa, K. O'Brien, T. Ono, P. I. Palmer, D. Pierrot, B. Poulter, L. Resplandy, E. Robertson, C. Rödenbeck, J. Schwinger, R. Séférian, I. Skjelvan, A. J. P. Smith, A. J. Sutton, T. Tanhua, P. P. Tans, H. Tian, B. Tilbrook, G. V. D. Werf, N. Vuichard, A. P. Walker, R. Wanninkhof, A. J. Watson, D. Willis, A. J. Wiltshire,

W. Yuan, X. Yue, S. Zaehle, Global Carbon Budget 2020. *Earth Syst. Sci. Data* **12**, 3269–3340 (2020).
3. G. Marland, Uncertainties in accounting for CO_2 from fossil fuels. *J. Ind. Ecol.* **12**, 136–139 (2008).
4. Nature Climate Change, The gigatonne gap in China's carbon dioxide inventories, www.nature.com/articles/nclimate1560.
5. Z. Liu, D. Guan, W. Wei, S. J. Davis, P. Ciais, J. Bai, S. Peng, Q. Zhang, K. Hubacek, G. Marland, R. J. Andres, D. Crawford-Brown, J. Lin, H. Zhao, C. Hong, T. A. Boden, K. Feng, G. P. Peters, F. Xi, J. Liu, Y. Li, Y. Zhao, N. Zeng, K. He, Reduced carbon emission estimates from fossil fuel combustion and cement production in China. *Nature* **524**, 335–338 (2015).
6. M. Crippa, G. Oreggioni, D. Guizzardi, M. Muntean, E. Schaaf, V. E. Lo, E. Solazzo, F. Monforti-Ferrario, J. Olivier, E. Vignati, Fossil CO_2 and GHG emissions of all world countries. 105, 10. 2760/687800, (2019).
7. S. Hogue, E. Marland, R. J. Andres, G. Marland, D. Woodard, Uncertainty in gridded CO_2 emissions estimates. *Earth's Fut.* **4**, 225–239 (2016).
8. M. Saunois, A. R. Stavert, B. Poulter, P. Bousquet, J. G. Canadell, R. B. Jackson, P. A. Raymond, E. J. Dlugokencky, S. Houweling, P. K. Patra, P. Ciais, V. K. Arora, D. Bastviken, P. Bergamaschi, D. R. Blake, G. Brailsford, L. Bruhwiler, K. M. Carlson, M. Carrol, S. Castaldi, N. Chandra, C. Crevoisier, P. M. Crill, K. Covey, C. L. Curry, G. Etiope, C. Frankenberg, N. Gedney, M. I. Hegglin, L. Höglund-Isaksson, G. Hugelius, M. Ishizawa, A. Ito, G. Janssens-Maenhout, K. M. Jensen, F. Joos, T. Kleinen, P. B. Krummel, R. L. Langenfelds, G. G. Laruelle, L. Liu, T. Machida, S. Maksyutov, K. C. McDonald, J. McNorton, P. A. Miller, J. R. Melton, I. Morino, J. Müller, F. Murguia-Flores, V. Naik, Y. Niwa, S. Noce, S. O'Doherty, R. J. Parker, C. Peng, S. Peng, G. P. Peters, C. Prigent, R. Prinn, M. Ramonet, P. Regnier, W. J. Riley, J. A. Rosentreter, A. Segers, I. J. Simpson, H. Shi, S. J. Smith, L. P. Steele, B. F. Thornton, H. Tian, Y. Tohjima, F. N. Tubiello, A. Tsuruta, N. Viovy, A. Voulgarakis, T. S. Weber, M. van Weele, G. R. van der Werf, R. F. Weiss, D. Worthy, D. Wunch, Y. Yin, Y. Yoshida, W. Zhang, Z. Zhang, Y. Zhao, B. Zheng, Q. Zhu, Q. Zhu, Q. Zhuang, The global methane budget 2000–2017. *Earth Syst. Sci. Data* **12**, 1561–1623 (2020).
9. E. G. Nisbet, M. R. Manning, E. J. Dlugokencky, R. E. Fisher, D. Lowry, S. E. Michel, C. L. Myhre, S. M. Platt, G. Allen, P. Bousquet, R. Brownlow, M. Cain, J. L. France, O. Hermansen, R. Hossaini, A. E. Jones, I. Levin, A. C. Manning, G. Myhre, J. A. Pyle, B. H. Vaughn, N. J. Warwick, J. W. C. White, Very strong atmospheric methane growth in the 4 years 2014–2017: Implications for the Paris Agreement. *Global Biogeochem. Cycles* **33**, 318–342 (2019).
10. A. J. Turner, C. Frankenberg, E. A. Kort, Interpreting contemporary trends in atmospheric methane. *Proc. Natl. Acad. Sci.* **116**, 2805–2813 (2019).
11. A. Voulgarakis, V. Naik, J.-F. Lamarque, D. T. Shindell, P. J. Young, M. J. Prather, O. Wild, R. D. Field, D. Bergmann, P. Cameron-Smith, I. Cionni, W. J. Collins, S. B. Dalsøren, R. M. Doherty, V. Eyring, G. Faluvegi, G. A. Folberth, L. W. Horowitz, B. Josse, I. A. MacKenzie, T. Nagashima, D. A. Plummer, M. Righi, S. T. Rumbold, D. S. Stevenson, S. A. Strode, K. Sudo, S. Szopa, G. Zeng, Analysis of present day and future OH and methane lifetime in the ACCMIP simulations. *Atmos. Chem. Phys.* **13**, 2563–2587 (2013).
12. D. J. Jacob, D. J. Varon, D. H. Cusworth, P. E. Dennison, C. Frankenberg, R. Gautam, L. Guanter, J. Kelley, J. McKeever, L. E. Ott, B. Poulter, Z. Qu, A. K. Thorpe, J. R. Worden, R. M. Duren, Quantifying methane emissions from the global scale down to point sources using satellite observations of atmospheric methane. *Atmos. Chem. Phys.* **22**, 9617–9646 (2022).
13. R. Voors, J. de Vries, I. S. Bhatti, D. Lobb, T. Wood, N. van der Valk, I. Aben, P. Veefkind, TROPOMI, the Sentinel 5 precursor instrument for air quality and climate observations: Status of the current design, in *International Conference on Space Optics—ICSO 2012* (SPIE, 2017), vol. 10564, pp. 442–446; www.spiedigitallibrary.org/conference-proceedings-of-spie/10564/105641Q/TROPOMI-the-Sentinel-5-precursor-instrument-for-air-quality-and/10.1117/12.2309017.full.
14. A. Eldering, T. E. Taylor, C. W. O'Dell, R. Pavlick, The OCO-3 mission: Measurement objectives and expected performance based on 1 year of simulated data. *Atmos. Meas. Tech.* **12**, 2341–2370 (2019).
15. D. R. Thompson, A. K. Thorpe, C. Frankenberg, R. O. Green, R. Duren, L. Guanter, A. Hollstein, E. Middleton, L. Ong, S. Ungar, Space-based remote imaging spectroscopy of the Aliso Canyon CH_4 superemitter. *Geophys. Res. Lett.* **43**, 6571–6578 (2016).
16. D. J. Varon, J. McKeever, D. Jervis, J. D. Maasakkers, S. Pandey, S. Houweling, I. Aben, T. Scarpelli, D. J. Jacob, Satellite discovery of anomalously large methane point sources from oil/gas production. *Geophys. Res. Lett.* **46**, 13507–13516 (2019).
17. D. J. Varon, D. J. Jacob, D. Jervis, J. McKeever, Quantifying time-averaged methane emissions from individual coal mine vents with GHGSat-D satellite observations. *Environ. Sci. Technol.* **54**, 10246–10253 (2020).
18. J. D. Maasakkers, D. J. Varon, A. Elfarsdóttir, J. McKeever, D. Jervis, G. Mahapatra, S. Pandey, A. Lorente, T. Borsdorff, L. R. Foorthuis, B. J. Schuit, P. Tol, T. A. van Kempen, R. van Hees, I. Aben, Using satellites to uncover large methane emissions from landfills. *Sci. Adv.* **8**, eabn9683 (2022).
19. D. H. Cusworth, R. M. Duren, A. K. Thorpe, Multisatellite imaging of a gas well blowout enables quantification of total methane emissions. *Geophys. Res. Lett.* **48**, e2020GL090864 (2020).
20. L. Guanter, I. Irakulis-Loitxate, J. Gorroño, E. Sánchez-García, D. H. Cusworth, D. J. Varon, S. Cogliati, R. Colombo, Mapping methane point emissions with the PRISMA spaceborne imaging spectrometer. *Remote Sens. Environ.* **265**, 112671 (2021).
21. D. J. Varon, D. Jervis, J. McKeever, I. Spence, D. Gains, D. J. Jacob, High-frequency monitoring of anomalous methane point sources with multispectral Sentinel-2 satellite observations. *Atmos. Meas. Tech.* **14**, 2771–2785 (2021).
22. T. Ehret, A. De Truchis, M. Mazzolini, J.-M. Morel, A. d'Aspremont, T. Lauvaux, R. Duren, D. Cusworth, G. Facciolo, Global tracking and quantification of oil and gas methane emissions from recurrent sentinel-2 imagery. *Environ. Sci. Technol.* **56**, 10517–10529 (2022).
23. E. Sánchez-García, J. Gorroño, I. Irakulis-Loitxate, D. J. Varon, L. Guanter, Mapping methane plumes at very high spatial resolution with the WorldView-3 satellite. *Atmos. Meas. Tech.* **15**, 1657–1674 (2022).
24. I. Irakulis-Loitxate, J. Gorroño, D. Zavala-Araiza, L. Guanter, Satellites detect a methane ultra-emission event from an offshore platform in the gulf of mexico. *Environ. Sci. Technol. Lett.* **9**, 520–525 (2022).
25. R. O. Green, N. Mahowald, D. R. Thompson, C. Ung, P. Brodrick, R. Pollock, M. Bennett, S. Lundeen, M. Joyce, W. Olson-Duvall, B. Oaida, Performance and early results from the Earth Surface Mineral Dust Source Investigation (EMIT) imaging spectroscopy mission, in *2023 IEEE Aerospace Conference* (IEEE, 2023), pp. 1–10.
26. R. O. Green, N. Mahowald, C. Ung, D. R. Thompson, L. Bator, M. Bennet, M. Bernas, N. Blackway, C. Bradley, J. Cha, P. Clark, R. Clark, D. Cloud, E. Diaz, E. Ben Dor, R. Duren, M. Eastwood, B. L. Ehlmann, L. Fuentes, P. Ginoux, J. Gross, Y. He, O. Kalashnikova, W. Kert, D. Keymeulen, M. Klimesh, D. Ku, H. Kwong-Fu, E. Liggett, L. Li, S. Lundeen, M. D. Makowski, A. Mazer, R. Miller, P. Mouroulis, B. Oaida, G. S. Okin, A. Ortega, A. Oyake, H. Nguyen, T. Pace, T. H. Painter, J. Pempejian, C. P. Garcia-Pando, T. Pham, B. Phillips, R. Pollock, R. Purcell, V. Realmuto, J. Schoolcraft, A. Sen, S. Shin, L. Shaw, M. Soriano, G. Swayze, E. Thingvold, A. Vaid, J. Zan, The earth surface mineral dust source investigation: An earth science imaging spectroscopy mission, in *2020 IEEE Aerospace Conference* (IEEE, 2020), pp. 1–15.
27. R. O. Green, M. L. Eastwood, C. M. Sarture, T. G. Chrien, M. Aronsson, B. J. Chippendale, J. A. Faust, B. E. Pavri, C. J. Chovit, M. Solis, M. R. Olah, O. Williams, Imaging spectroscopy and the Airborne Visible/Infrared Imaging Spectrometer (AVIRIS). *Remote Sens. Environ.* **65**, 227–248 (1998).
28. D. A. Roberts, E. S. Bradley, R. Cheung, I. Leifer, P. E. Dennison, J. S. Margolis, Mapping methane emissions from a marine geological seep source using imaging spectrometry. *Remote Sens. Environ.* **114**, 592–606 (2010).
29. A. K. Thorpe, D. A. Roberts, E. S. Bradley, C. C. Funk, P. E. Dennison, I. Leifer, High resolution mapping of methane emissions from marine and terrestrial sources using a cluster-tuned matched filter technique and imaging spectrometry. *Remote Sens. Environ.* **134**, 305–318 (2013).
30. A. K. Thorpe, R. Duren, S. Conley, K. Prasad, B. Bue, V. Yadav, K. Foster, T. Rafiq, F. Hopkins, M. Smith, M. L. Fischer, D. Thompson, C. Frankenberg, I. McCubbin, M. Eastwood, R. Green, C. E. Miller, Methane emissions from underground gas storage in California. *Environ. Res. Lett.* **15**, 045005 (2020).
31. L. Hamlin, R. O. Green, P. Mouroulis, M. Eastwood, D. Wilson, M. Dudik, C. Paine, Imaging spectrometer science measurements for terrestrial ecology: AVIRIS and new developments, in *IEEE Aerospace Conference Proceedings* (IEEE, 2011), pp. 1–7.
32. G. P. Asner, D. E. Knapp, T. Kennedy-Bowdoin, M. O. Jones, R. E. Martin, J. W. Boardman, C. B. Field, Carnegie Airborne Observatory: In-flight fusion of hyperspectral imaging and waveform light detection and ranging for three-dimensional studies of ecosystems. *J. Appl. Remote Sens.* **1**, 013536 (2007).
33. C. Frankenberg, A. K. Thorpe, D. R. Thompson, G. Hulley, E. A. Kort, N. Vance, J. Borchardt, T. Krings, K. Gerilowski, C. Sweeney, S. Conley, B. D. Bue, A. D. Aubrey, S. Hook, R. O. Green, Airborne methane remote measurements reveal heavytail flux distribution in Four Corners region. *Proc. Natl. Acad. Sci. U.S.A.* **113**, 9734–9739 (2016).
34. D. H. Cusworth, R. M. Duren, A. K. Thorpe, W. Olson-Duvall, J. Heckler, J. W. Chapman, M. L. Eastwood, M. C. Helmlinger, R. O. Green, G. P. Asner, P. E. Dennison, C. E. Miller, Intermittency of large methane emitters in the permian basin. *Environ. Sci. Technol. Lett.* **8**, 567–573 (2021).
35. D. H. Cusworth, A. K. Thorpe, A. K. Ayasse, D. Stepp, J. Heckler, G. P. Asner, C. E. Miller, V. Yadav, J. W. Chapman, M. L. Eastwood, R. O. Green, B. Hmiel, D. R. Lyon, R. M. Duren, Strong methane point sources contribute a disproportionate fraction of total emissions across multiple basins in the United States. *Proc. Natl. Acad. Sci.* **119**, e2202338119 (2022).
36. A. K. Ayasse, A. K. Thorpe, D. H. Cusworth, E. A. Kort, A. G. Negron, J. Heckler, G. Asner, R. M. Duren, Methane remote sensing and emission quantification of offshore shallow water oil and gas platforms in the Gulf of Mexico. *Environ. Res. Lett.* **17**, 084039 (2022).

37. J. Borchardt, K. Gerilowski, S. Krautwurst, H. Bovensmann, A. K. Thorpe, D. R. Thompson, C. Frankenberg, C. E. Miller, R. M. Duren, J. P. Burrows, Detection and quantification of CH_4 plumes using the WFM-DOAS retrieval on AVIRIS-NG hyperspectral data. *Atmos. Meas. Tech.* **14**, 1267–1291 (2021).
38. M. D. Foote, P. E. Dennison, A. K. Thorpe, D. R. Thompson, S. Jongaramrungruang, C. Frankenberg, S. C. Joshi, Fast and accurate retrieval of methane concentration from imaging spectrometer data using sparsity prior. *IEEE Trans. Geosci. Remote Sens.* **58**, 6480–6492 (2020).
39. D. H. Cusworth, R. Duren, A. K. Thorpe, E. Tseng, D. Thompson, A. Guha, S. Newman, K. Foster, C. E. Miller, Using remote sensing to detect, validate, and quantify methane emissions from California solid waste operations. *Environ. Res. Lett.* **15**, 054012 (2020).
40. R. M. Duren, A. K. Thorpe, K. T. Foster, T. Rafiq, F. M. Hopkins, V. Yadav, B. D. Bue, D. R. Thompson, S. Conley, N. K. Colombi, C. Frankenberg, I. B. McCubbin, M. L. Eastwood, M. Falk, J. D. Herner, B. E. Croes, R. O. Green, C. E. Miller, California's methane super-emitters. *Nature* **575**, 180–184 (2019).
41. S. Jeong, M. L. Fischer, H. Breunig, A. R. Marklein, F. M. Hopkins, S. C. Biraud, Artificial intelligence approach for estimating dairy methane emissions. *Environ. Sci. Technol.* **56**, 4849–4858 (2022).
42. C. D. Elder, D. R. Thompson, A. K. Thorpe, P. Hanke, K. M. Walter Anthony, C. E. Miller, Airborne mapping reveals emergent power law of arctic methane emissions. *Geophys. Res. Lett.* **47**, e85707 (2020).
43. C. D. Elder, D. R. Thompson, A. K. Thorpe, H. A. Chandanpurkar, P. J. Hanke, N. Hasson, S. R. James, B. J. Minsley, N. J. Pastick, D. Olefeldt, K. M. Walter Anthony, C. E. Miller, Characterizing methane emission hotspots from thawing permafrost. *Global Biogeochem. Cycles* **35**, e2020GB006922 (2021).
44. P. E. Dennison, A. K. Thorpe, E. R. Pardyjak, D. A. Roberts, Y. Qi, R. O. Green, E. S. Bradley, C. C. Funk, High spatial resolution mapping of elevated atmospheric carbon dioxide using airborne imaging spectroscopy: Radiative transfer modeling and power plant plume detection. *Remote Sens. Environ.* **139**, 116–129 (2013).
45. A. K. Thorpe, C. Frankenberg, D. R. Thompson, R. M. Duren, A. D. Aubrey, B. D. Bue, R. O. Green, K. Gerilowski, T. Krings, J. Borchardt, E. A. Kort, C. Sweeney, S. Conley, D. A. Roberts, P. E. Dennison, Airborne DOAS retrievals of methane, carbon dioxide, and water vapor concentrations at high spatial resolution: Application to AVIRIS-NG. *Atmos. Meas. Tech.* **10**, 3833–3850 (2017).
46. D. H. Cusworth, R. M. Duren, A. K. Thorpe, M. L. Eastwood, R. O. Green, P. E. Dennison, C. Frankenberg, J. W. Heckler, G. P. Asner, Quantifying global power plant carbon dioxide emissions with imaging spectroscopy. *AGU Advances* **2**, e2020AV000350 (2021).
47. F. A. Kruse, A. B. Lefkoff, J. B. Dietz, Expert system-based mineral mapping in northern death valley, California/Nevada, using the Airborne Visible/Infrared Imaging Spectrometer (AVIRIS). *Remote Sens. Environ.* **44**, 309–336 (1993).
48. G. A. Swayze, K. S. Smith, R. N. Clark, S. J. Sutley, R. M. Pearson, J. S. Vance, P. L. Hageman, P. H. Briggs, A. L. Meier, M. J. Singleton, S. Roth, Using imaging spectroscopy to map acidic mine waste. *Environ. Sci. Technol.* **34**, 47–54 (2000).
49. D. A. Roberts, M. Gardner, R. Church, S. Ustin, G. Scheer, R. O. Green, Mapping chaparral in the Santa Monica mountains using multiple endmember spectral mixture models. *Remote Sens. Environ.* **65**, 267–279 (1998).
50. G. P. Asner, Biophysical and biochemical sources of variability in canopy reflectance. *Remote Sens. Environ.* **64**, 234–253 (1998).
51. J. M. Jaquet, F. Schanz, P. Bossard, K. Hanselmann, F. Gendre, Measurements and significance of bio-optical parameters for remote sensing in two subalpine lakes of different trophic state. *Aquat. Sci.* **56**, 263–303 (1994).
52. L. L. Richardson, D. Buisson, L. Cheng-Jen, V. Ambrosia, The detection of algal photosynthetic accessory pigments using airborne visible-infrared imaging spectrometer (AVIRIS) spectral data. *Mar. Technol. Soc. J.* **28**, 10–21 (1994).
53. A. W. Nolin, J. Dozier, Estimating snow grain size using AVIRIS data. *Remote Sens. Environ.* **44**, 231–238 (1993).
54. T. H. Painter, D. A. Roberts, R. O. Green, J. Dozier, The effect of grain size on spectral mixture analysis of snow-covered area from AVIRIS data. *Remote Sens. Environ.* **65**, 320–332 (1998).
55. D. R. Thompson, R. O. Green, C. Bradley, P. G. Brodrick, B. Dor, M. Bennett, M. Bernas, N. Carmon, K. D. Chadwick, R. N. Clark, R. W. Coleman, E. Cox, E. Diaz, M. L. Eastwood, R. Eckert, B. Ehlmann, P. Ginoux, M. G. Ageitos, K. Grant, L. Guanter, D. H. Pearlshtien, M. Helmlinger, H. Herzog, T. Hoefen, Y. Huang, A. Keebler, O. Kalashnikova, D. Keymeulen, R. Kokaly, M. Klose, L. Li, S. Lundeen, N. Mahowald, J. Meyer, E. Middleton, R. L. Miller, P. Mouroulis, B. Oaida, V. Obiso, F. Ochoa, W. Olson-Duvall, G. S. Okin, T. H. Painter, C. P. García-Pando, V. Realmuto, L. Shaw, P. Sullivan, E. Thingvold, A. K. Thorpe, G. Swayze, S. Vannan, C. Villarreal, H. R. Pollock, C. Ung, D. W. Wilson, S. Zandbergen, On-orbit calibration and performance of the EMIT imaging spectrometer. *ESS Open Archive* 10.22541/essoar.168988432.29040205/v1, (2023).
56. T. R. Scarpelli, D. J. Jacob, S. Grossman, X. Lu, Z. Qu, M. P. Sulprizio, Y. Zhang, F. Reuland, D. Gordon, J. R. Worden, Updated Global Fuel Exploitation Inventory (GFEI) for methane emissions from the oil, gas, and coal sectors: Evaluation with inversions of atmospheric methane observations. *Atmos. Chem. Phys.* **22**, 3235–3249 (2022).
57. T. Hill, R. Nassar, Pixel size and revisit rate requirements for monitoring power plant CO_2 emissions from space. *Remote Sens.* **11**, 1608 (2019).
58. World Resources Institute, Global Power Plant Database - Data, https://datasets.wri.org/dataset/globalpowerplantdatabase.
59. Global Energy Monitor, Tracker Map, https://globalenergymonitor.org/projects/global-coal-plant-tracker/tracker/.
60. S. Kaza, L. C. Yao, P. Bhada-Tata, F. Van Woerden, *What a Waste 2.0: A Global Snapshot of Solid Waste Management to 2050* (World Bank, 2018); https://openknowledge.worldbank.org/handle/10986/30317.
61. L. Höglund-Isaksson, A. Gómez-Sanabria, Z. Klimont, P. Rafaj, W. Schöpp, Technical potentials and costs for reducing global anthropogenic methane emissions in the 2050 timeframe—Results from the GAINS model. *Environ. Res. Commun.* **2**, 025004 (2020).
62. Iran-Germany Waste Management Initiative, The introduction of complex waste processing and disposal Arad Kooh & kahrizak, www.igwmi.com/page_688.html.
63. M. I. Al-Wabel, W. S. Al Yehya, A. S. AL-Farraj, S. E. El-Maghraby, Characteristics of landfill leachates and bio-solids of municipal solid waste (MSW) in Riyadh City, Saudi Arabia. *J. Saudi Soc. Agric. Sci.* **10**, 65–70 (2011).
64. GE News, GE Steam Turbines to Boost Output, Efficiency at SEC PP10 Power Plant; a Key to Meeting Saudi Arabia's Growing Power Demands, www.ge.com/news/press-releases/ge-steam-turbines-boost-output-efficiency-sec-pp10-power-plant-key-meeting-saudi-1.
65. T. N. Lavoie, P. B. Shepson, C. A. Gore, B. H. Stirm, R. Kaeser, B. Wulle, D. Lyon, J. Rudek, Assessing the methane emissions from natural gas-fired power plants and oil refineries. *Environ. Sci. Tech.* **51**, 3373–3381 (2017).
66. K. D. Hajny, O. E. Salmon, J. Rudek, D. R. Lyon, A. A. Stuff, B. H. Stirm, R. Kaeser, C. R. Floerchinger, S. Conley, M. L. Smith, P. B. Shepson, Observations of methane emissions from natural gas-fired power plants. *Environ. Sci. Tech.* **53**, 8976–8984 (2019).
67. A. K. Thorpe, E. A. Kort, D. H. Cusworth, A. K. Ayasse, B. D. Bue, V. Yadav, D. R. Thompson, C. Frankenberg, J. Herner, M. Falk, R. O. Green, C. E. Miller, R. M. Duren, Methane emissions decline from reduced oil, natural gas, and refinery production during COVID-19. *Environ. Res. Commun.* **5**, 021006 (2023).
68. Shedgum-Yanbu NGL Pipeline, www.gem.wiki/Shedgum-Yanbu_NGL_Pipeline.
69. EDX, Development of an open global oil and gas infrastructure inventory and geodatabase, https://edx.netl.doe.gov/dataset/development-of-an-open-global-oil-and-gas-infrastructure-inventory-and-geodatabase.
70. J. R. Worden, D. H. Cusworth, Z. Qu, Y. Yin, Y. Zhang, A. A. Bloom, S. Ma, B. K. Byrne, T. Scarpelli, J. D. Maasakkers, D. Crisp, R. Duren, D. J. Jacob, The 2019 methane budget and uncertainties at 1° resolution and each country through Bayesian integration of GOSAT total column methane data and a priori inventory estimates. *Atmos. Chem. Phys.* **22**, 6811–6841 (2022).
71. X. Lu, D. J. Jacob, Y. Zhang, J. D. Maasakkers, M. P. Sulprizio, L. Shen, Z. Qu, T. R. Scarpelli, H. Nesser, R. M. Yantosca, J. Sheng, A. Andrews, R. J. Parker, H. Boesch, A. A. Bloom, S. Ma, Global methane budget and trend, 2010–2017: Complementarity of inverse analyses using in situ (GLOBALVIEWplus CH_4 ObsPack) and satellite (GOSAT) observations. *Atmos. Chem. Phys.* **21**, 4637–4657 (2021).
72. International - U.S. Energy Information Administration (EIA), www.eia.gov/international/analysis/world.
73. T. Lauvaux, C. Giron, M. Mazzolini, A. d'Aspremont, R. Duren, D. Cusworth, D. Shindell, P. Ciais, Global assessment of oil and gas methane ultra-emitters. *Science* **375**, 557–561 (2022).
74. I. Irakulis-Loitxate, L. Guanter, J. D. Maasakkers, D. Zavala-Araiza, I. Aben, Satellites detect abatable super-emissions in one of the world's largest methane hotspot regions. *Environ. Sci. Tech.* **56**, 2143–2152 (2022).
75. A. K. Thorpe, C. Frankenberg, D. A. Roberts, Retrieval techniques for airborne imaging of methane concentrations using high spatial and moderate spectral resolution: Application to AVIRIS. *Atmos. Meas. Tech.* **7**, 491–506 (2014).
76. D. R. Thompson, I. Leifer, H. Bovensmann, M. Eastwood, M. Fladeland, C. Frankenberg, K. Gerilowski, R. O. Green, S. Kratwurst, T. Krings, B. Luna, A. K. Thorpe, Real-time remote detection and measurement for airborne imaging spectroscopy: A case study with methane. *Atmos. Meas. Tech.* **8**, 4383–4397 (2015).
77. H. Hersbach, B. Bell, P. Berrisford, G. Biavati, A. Horányi, J. Muñoz Sabater, J. Nicolas, C. Peubey, R. Radu, I. Rozum, D. Schepers, A. Simmons, C. Soci, D. Dee, J.-N.Thépaut, *ERA5 hourly data on single levels from 1940 to present. Copernicus Climate Change Service (C3S)* (Climate Data Store, 2023).
78. A. K. Thorpe, C. O'Handley, G. D. Emmitt, P. L. DeCola, F. M. Hopkins, V. Yadav, A. Guha, S. Newman, J. D. Herner, M. Falk, R. M. Duren, Improved methane emission estimates using AVIRIS-NG and an Airborne Doppler Wind Lidar. *Remote Sens. Environ.* **266**, 112681 (2021).

79. D. J. Varon, D. J. Jacob, J. McKeever, D. Jervis, B. O. A. Durak, Y. Xia, Y. Huang, Quantifying methane point sources from fine-scale satellite observations of atmospheric methane plumes. *Atmos. Meas. Tech.* **11**, 5673–5686 (2018).
80. E. D. Sherwin, J. S. Rutherford, Y. Chen, S. Aminfard, E. A. Kort, R. B. Jackson, A. R. Brandt, Single-blind validation of space-based point-source detection and quantification of onshore methane emissions. *Sci. Rep.* **13**, 3836 (2023).
81. P. G. Brodrick, J. Fahlen, R. W. Coleman, B. Bue, D. R. Thompson, A. K. Thorpe, emit-sds/emit-ghg: v0.0.0 (v0.0.0). Zenodo, doi:https://doi.org/10.5281/zenodo.8156665.
82. F. Calef, T. Soliman, NASA-AMMOS MMGIS open source software (2023); https://github.com/NASA-AMMOS/MMGIS.

Acknowledgments: We would like to acknowledge the contributions of the entire EMIT engineering and science teams and the ISS team for enabling the EMIT mission. We thank NASA's Earth Science Division with special thanks to J. Kaye for continued support of the greenhouse gas application. The EMIT greenhouse gas application online mapping tool was developed by the JPL MMGIS team. Additional support was provided by Carbon Mapper, the University of Arizona, NASA's Carbon Monitoring System, the Rocky Mountain Institute (RMI), the Environmental Defense Fund (EDF), and others. This work was undertaken in part at the JPL, California Institute of Technology, under a contract with NASA (80NM0018D0004). **Funding:** This study was supported by funding provided by both the JPL and NASA's Earth Science Division. **Author contributions:** Conceptualization: A.K.T., R.O.G., D.R.T., R.M.D., C.F., L.G., P.E.D., D.A.R., M.L.E., and C.E.M. Methodology: A.K.T., R.M.D., D.H.C., D.R.T., P.G.B., and A.K.A. Investigation: A.K.T., I.I.-L., J.W.C., and C.D.E. Visualization: A.K.T. and P.G.B. Supervision: A.K.T. and K.D.C. Writing (original draft): A.K.T., P.G.B., C.D.E., D.R.T., and P.G.B.. Writing (review and editing): A.K.T., C.D.E., D.R.T., P.G.B., J.R.W., R.M.D., P.E.D., D.A.R., L.G., I.I.-L., C.E.M., and J.E.F. **Competing interests:** The authors declare that they have no competing interests. **Data and materials availability:** All data needed to evaluate the conclusions in the paper are present in the paper and/or the Supplementary Materials. All EMIT radiance data are available through the LP DAAC at the following link: https://lpdaac.usgs.gov/products/emitl1bradv001. All codes are available at https://doi.org/10.5281/zenodo.8156665 (*81*), https://github.com/emit-sds, and https://github.com/emit-sds/emit-ghg. The plume examples presented in this study are available through the EMIT applications online mapping tool (https://earth.jpl.nasa.gov/emit/data/data-portal/Greenhouse-Gases/) with periodic updates reflecting additional observed emissions.

Submitted 18 February 2023
Accepted 17 October 2023
Published 17 November 2023
10.1126/sciadv.adh2391